ELSEVIER

International Journal of Mass Spectrometry 192 (1999) 27–37

International Journal of Mass Spectrometry

# Electron-impact ionization of $Fe^{5+}$ ions

M. Stenke, K. Aichele, D. Hathiramani, E. Salzborn*

*Institut für Kernphysik, Strahlenzentrum, Universität Giessen, 35392 Giessen, Germany*

Received 7 December 1998; accepted 22 March 1999

**Abstract**

Employing the dynamic crossed-beams technique, absolute cross sections for single, double, and triple ionization of $Fe^{5+}$ ions by electron impact have been measured from the threshold up to 1 keV, partly up to 5 keV. The data for single ionization are in very good agreement with configuration-average distorted-wave (CADW) calculations if excitation-autoionization processes are taken into account. The results for double and triple ionization are in poor agreement with semiempirical predictor formulae. Using a high resolution energy-scan technique, we have studied narrow resonances in the double ionization cross section in the energy range from 560–940 eV. Besides contributions from excitation-double-autoionization processes, a remarkable number of structures arising from resonant-excitation-triple-autoionization processes could be observed. (Int J Mass Spectrom 192 (1999) 27–37) © 1999 Elsevier Science B.V.

*Keywords:* Electron-impact ionization; Ions; Cross sections

## 1. Introduction

Cross sections for the electron-impact ionization of ions are essential for the analysis of hot astrophysical and laboratory plasmas. A wide range of elements and stages of ionization may be involved. For quantitative modeling of structure and dynamics of fusion plasmas knowledge of the cross sections for the species encountered in the plasma is necessary. Here cross sections of iron as a major constituent of stainless steel in the reactor wall are very important. Iron is also important as an abundant element in astrophysical plasmas. Direct ionization of an outer-shell electron as pictured by

$$e^- + A^{q+} \rightarrow A^{(q+1)+} + 2e^-$$

is generally assumed to be the dominating contribution to the total cross section for single ionization. However, in the last decade experiment and theory have shown that indirect processes like excitation autoionization (EA)

$$e^- + A^{q+} \rightarrow [A^{q+}]^* + e^-$$
$$\downarrow$$
$$[A^{q+}]^* \rightarrow A^{(q+1)+} + e^-$$

may contribute substantially to the electron-impact ionization of transition metal ions, especially in low stages of ionization. Sudden changes in the indirect contributions may be observed along isoelectronic and isonuclear sequences. Ions with an open $3d$ shell

* Corresponding author.


*PII* S1387-3806(99)00095-0

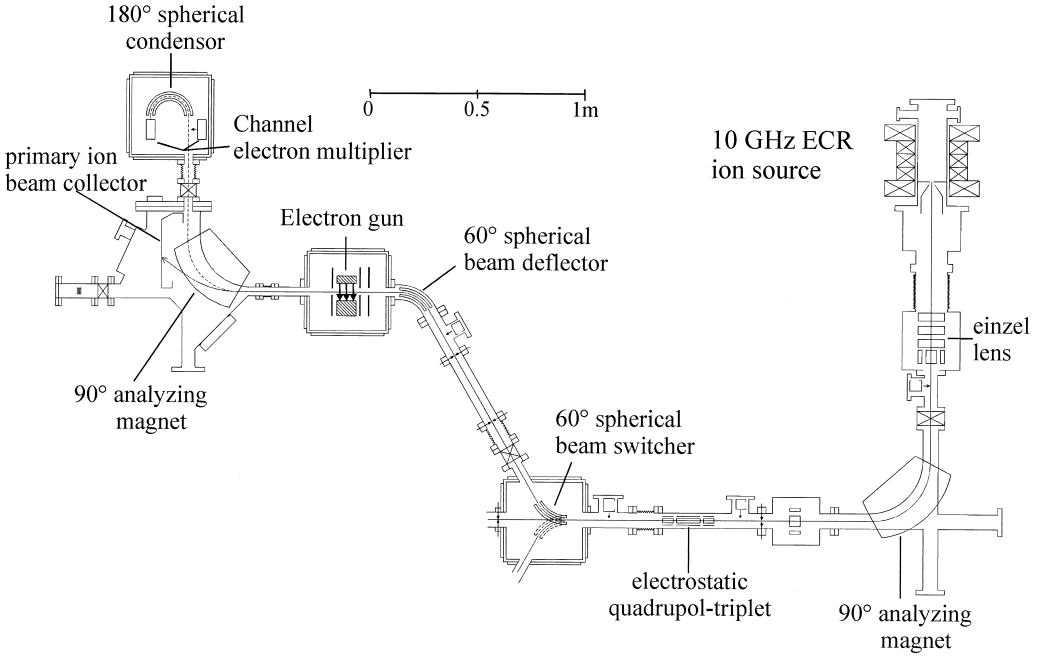


Fig. 1. Diagram of the experimental setup, including the whole beamline from the ion source to the single particle detector.

in the ground state configuration like $Fe^{5+}$ ($[Ne]3s^2 3p^6 3d^3$) provide a good test case to acquire more knowledge about EA contributions to the single ionization cross section of transition metal ions.

It has been convincingly shown by Tendler et al. [1] that effects of multiple ionization processes on the charge state evolution of the impurities in fusion plasmas can be neglected in the coronal equilibrium. On the other hand, if neutrals or ions in low charge states are suddenly exposed to high electron temperatures, multiple ionization processes strongly influence the charge state evolution and have to be taken into account [2,3]. Because of a small reaction rate, multiple ionization was not often experimentally studied in the past and on the theoretical side, general approaches on the basis of quantum mechanics to predict cross sections for multiple ionization are still unknown. However, some predictor formulae based on semiempirical approaches have been proposed [4–6]. In the case of multiple ionization, it is also interesting to explore the contributions to the total cross section from indirect processes such as excitation double autoionization (EDA) or resonant excitation triple autoionization (RETA), which is pictured by

$$e^- + A^{q+} \rightarrow [A^{(q-1)+}]^{**}$$
$$\downarrow$$
$$[A^{(q-1)+}]^{**} \rightarrow A^{(q+2)+} + 3e^-$$

Whereas the single ionization of iron ions was studied before both experimentally [7–11] and theoretically (a brief review is given in [12]), double and triple ionization processes have not been studied up to now.

## 2. Experimental technique

The present work was performed using the Giessen electron-ion crossed-beams facility shown in Fig. 1. The transmission of the ion beam through the experimental set up has been optimized using the GIOS ion optics calculation program [13]. A computer simula-

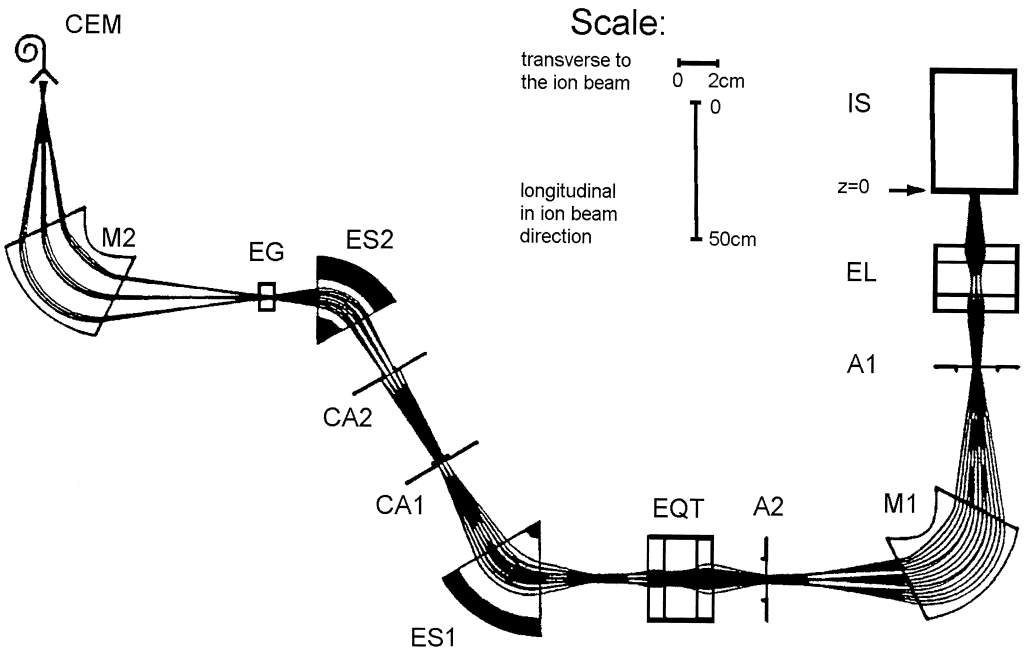


Fig. 2. Computer simulation of the horizontal ion beam trajectories in the beam transport system shown in Fig. 1 using the GIOS ion optic calculation program [13]. Starting point is $z = 0$, where the extraction hole of the ion source is placed. IS, ion source; EL, einzel lens; A1, A2, variable apertures; M1, M2, double-focusing analyzing magnets (90° deflection angle, 25 cm deflection radius); EQT, electrostatic quadrupole triplet; ES1, electrostatic spherical condenser (20 cm deflection radius); CA1, CA2, collimating apertures; ES2, electrostatic spherical condenser (17 cm deflection radius); EG, electron gun; CEM, single-particle detector.

tion of ion beam trajectories in the beam transport system is shown in Fig. 2.

The iron ions were produced in the plasma of a 10 GHz electron-cyclotron-resonance (ECR) ion source (IS) using the insertion technique. A bundle of thin (0.5 mm diameter) iron wires mounted on top of a remote controlled rod was fed axially to the edge of the ECR plasma discharge. By evaporation and sputtering, iron atoms were diffused into the plasma and successively ionized to higher charge stages by plasma electrons. After extraction at 10 kV acceleration voltage, beam focusing by an einzel lens (EL) and a first collimation (A1, A2), the ion beam was analyzed by a 90° double focusing (transversal and vertical to the ion beam direction) magnet (M1) to the desired mass-to-charge ratio. An electrostatic quadrupole triplet (EQT) was used for focusing before the beam was deflected by a 60° spherical beam switcher (ES1). Then the beam was tightly collimated by two apertures (CA1, CA2) to typically 1–2 mm diameter. A further beam deflection by a spherical beam condenser (ES2) was used to clean the ion beam before it was crossed at a 90° angle with an intense electron beam from an electron gun (EG). After the interaction the product ions were separated from the parent ion beam by a second 90° double focusing magnet (M2) and detected by a channel electron multiplier (CEM). In order to obtain a better signal-to-noise ratio, a further 180° spherical condenser can be used for an alternative detection of the product ions, especially for single ionization, where the background due to stripping reactions of the primary ions with residual gas is higher. Typical ion beam currents in the interaction region were 10 nA of $Fe^{5+}$.

For the measurements we employed two different types of electron guns. The first type is a high-current electron gun that delivers a ribbon-shaped electron beam at energies from 10–1000 eV and currents of up

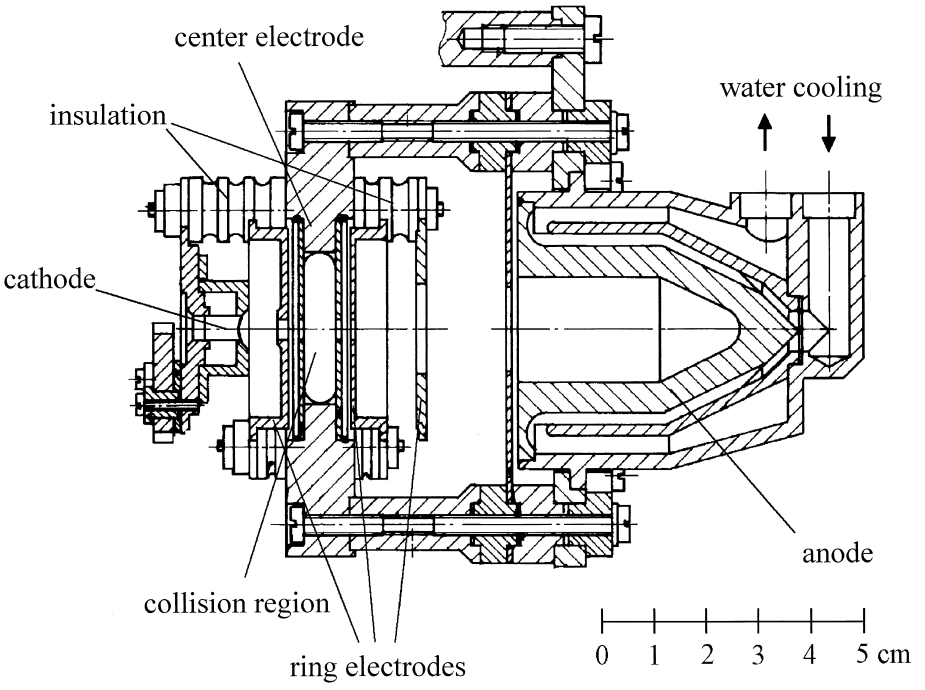


Fig. 3. Schematic view of the high-energy electron gun.

to 450 mA at 1 keV. This electron gun has been described in detail before [14].

The second type is a high-energy electron gun. This gun was specially designed [15] by the SLAC-166 trajectory code [16] for high voltages. It has an axially symmetric set up (Fig. 3). Calculated equipotential lines and electron trajectories in a longitudinal section of the electron gun are shown in Fig. 4. The electrons are emitted from an indirect heated tungsten dispenser cathode (C) at a potential $-U_i$. The cathode of 5 mm diameter is surrounded by a Pierce angle electrode. After acceleration by a ring-shaped elec-

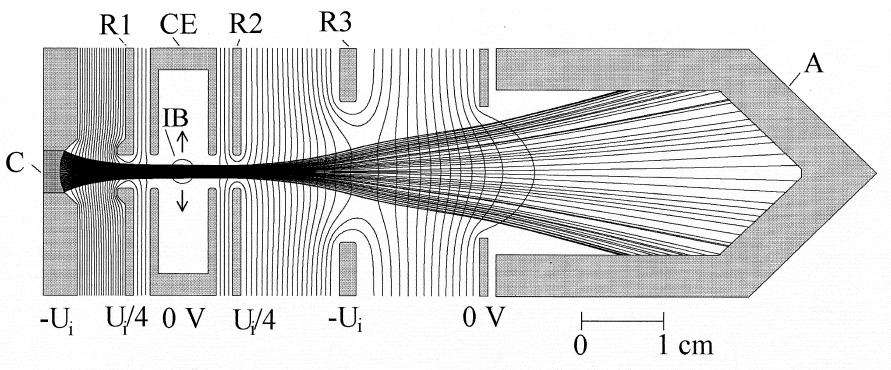


Fig. 4. Calculated equipotential lines and electron trajectories in a longitudinal section of the electron gun. C, cathode; R1, R2, R3, ring electrodes; CE, center electrode; IB, ion beam; A, water-cooled anode. All electrodes except the center electrode, which is a rectangular tube along the path of the ion beam, are axially symmetric. The potentials applied to the electrodes are given in terms of the voltage $U_i$ between the collision region and the cathode.

trode (R1) at positive potential $+U_i/4$, the electron beam with a diameter of 2 mm enters the interaction region with the ion beam, which is surrounded by a center electrode (CE) at ground potential. This electrode is a rectangular tube rather than a ring-shaped electrode and has two holes for the intersecting electron beam. In order to provide a shielding of potentials from the leads to other electrodes for the ion beam, the center electrode extends along the path of the ion beam. The collision energy is defined by the voltage $U_i$ between the cathode and the interaction region. Downstream of the interaction region is another electrode (R2) at potential $+U_i/4$. By means of an electrode (R3) at cathode potential $-U_i$ the beam is defocused before it enters the electron collector. In addition, the defocusing electrode acts as a screening electrode and prevents secondary electrons from escaping the collector anode ($A$) at ground potential. The measured electron current rises from 1 mA at 100 eV to 430 mA at 6.5 keV electron energy. The high energy gun delivers an electron current of 15.6 mA at 1 keV, whereas the high current gun reaches 450 mA. The electron current density in the collision region exceeds 10 A/cm$^2$ at maximum energy. Thus, the defocusing electrode is essential for dissipating the transported power of up to 2.8 kW onto a large surface inside the electron collector, which is provided with effective water cooling.

For the measurements of the absolute cross sections we employed the dynamic crossed-beams technique described by Müller et al. [17], where the electron gun is moved up and down through the ion beam with simultaneous registration of the ionization signal and both actual beam currents. The total experimental uncertainties of the measured cross sections are typically 8% at the maximum resulting from the root mean square of the nonstatistical errors of about 7.8% (ion detection efficiency $\pm 3\%$; ion and electron current $\pm 5\%$; ion and electron velocity $\pm 1\%$; and channel width $\pm 1\%$) and the statistical error at 95% confidence level. In this mode the reproducibility for the cross section is 1% at best. This limit is probably due to changes in the beam intensity profiles during a cross section measurement that cannot easily be accounted for by the technique described above. Thus, it is difficult to detect fine structures in total ionization cross sections caused by the presence of indirect ionization processes.

For a high resolution measurement we use another possible mode, the energy-scan technique [18]. In this mode both beams are fixed in optimum beam overlap position. Now we measure again the same parameters as above, however, we apply a very fast variation of the electron energy in steps of typically 0.04 eV and measurement times of 3 ms. By repeating scans many times, we average out possible fluctuations in the beam overlap, in the measurements of beam currents and counting rates, and in other sources of data scatter. It has been shown that this technique allows a precision that is at least a hundred times higher than obtained by the dynamic crossed-beams technique described above. Fluctuations in measured cross sections could be reduced to the 0.01% level [19]. This method is only a relative measurement, but by applying both modes we obtain a very high resolution of absolute cross sections by matching the energy-scan measurement to the data achieved by the dynamic technique.

Employing the fast energy-scan technique we have measured the cross section for the triple ionization of $Ba^{2+}$ ([Kr]$4d^{10}5s^25p^6$ ground state configuration) ions in the energy range 770–810 eV (Fig. 5). Pronounced peaks can be seen. These peaks result from a resonant dielectronic capture of the projectile electron into the parent $Ba^{2+}$ ion with simultaneous excitation of a core electron from the $3d$ subshell and subsequent emission of four electrons. These resonances give a contribution of 2.5% to the total cross section of 3.3 $10^{-18}$ cm$^2$ for triple ionization of $Ba^{2+}$. In Fig. 5(a) measurements with the high-energy gun are shown and in Fig. 5(b) measurements with the high-current gun are shown. In both cases the energy resolution is about 3 eV at 780 eV electron energy. The contribution of nonresonant ionization processes to the cross section has been approximated by a straight line and substracted. For determination of the electron energy spread a set of six Gaussians is fitted to the experimental data by means of a least square method. The resulting fit curve gives a good description of the experimental data. The fitted widths of the

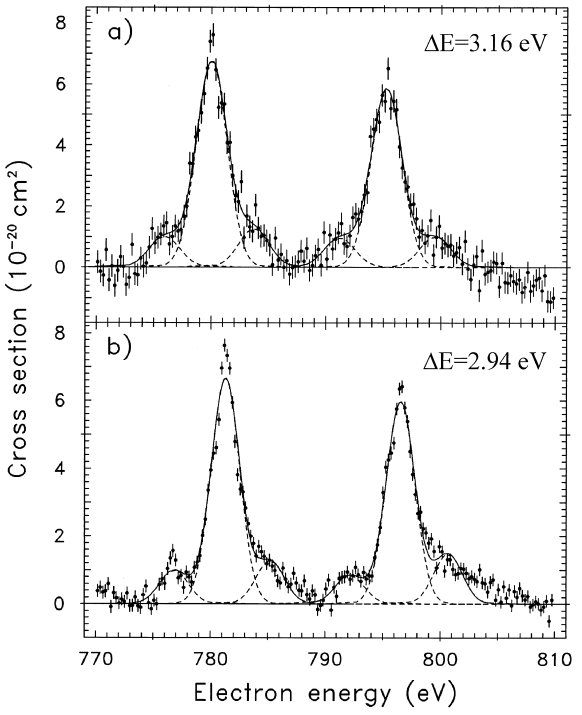


Fig. 5. Resonances in the cross section for the triple ionization of $Ba^{2+}$ ions. The contribution of nonresonant ionization processes to the cross section has been substracted. Error bars represent the statistical error. Results obtained with the high-energy electron gun (a) are compared with earlier measurements employing our high-current electron gun (b). A fitted set of six Gaussian distributions gives a good representation of the experimental data. The fitted widths of the Gaussians at 780 eV are 3.16 eV FWHM for the high-energy and 2.94 eV FWHM for the high-current electron gun, respectively.

profiles of 3.16 eV (FWHM) for the high-energy gun and 2.94 eV full width at half maximum for the high-current gun show no really significant differences in the spread of the electron energy distribution between the two guns. The small shift of 1.2 eV between the two data sets is in the uncertainty range of the absolute energy. The error bars represent the statistical error only.

## 3. Results and discussion

The results of the present cross section measurements for electron-impact ionization of $Fe^{5+}$ ions are shown in Figs. 6–8. The absolute cross sections are plotted as a function of the electron energy. The error bars indicate the total experimental uncertainties and the arrows show the ground state ionization thresholds. Using the multiconfigurational Dirac–Fock code by Grant et al. [20,21] we have calculated some threshold energies for inner-shell ionization and excitation energies of some configurations relative to the ground state configuration of $Fe^{5+}$ ($3s^2 3p^6 3d^3$) that may contribute by indirect processes to the cross section. Because of the vast number of possible configurations we only calculated a few of the more important states. The results are shown in Tables 1 and 2.

### 3.1. Single ionization

The measured cross section for electron-impact single ionization of $Fe^{5+}$ is displayed in Fig. 6 together with the data of Gregory et al. [9]. Both measurements are in very good agreement. The calculated ionization threshold is 98.7 eV [12,22] for the $Fe^{5+}$ ($3s^2 3p^6 3d^3$) ground state configuration. In both measured cross sections only a small ionization signal below the ground state ionization threshold and, thus, a rather small contribution of ions in long-lived metastable states is observed.

The measurements are compared to the well known semiempirical Lotz formula [23] (dashed-dotted curve) and to configuration-average distorted-wave (CADW) calculations (full and dashed curve) by Pindzola et al. [12]. The CADW calculations were computed for direct ionization (dashed curve) and, additionally, excitation-autoionization processes were included in the calculation (full curve). For all curves $3d$, $3p$, and $3s$ shell ionization is included, visible partly as a bend in the ionization curves at about 150 eV ($3p$ ionization threshold). Both the Lotz formula as well as the CADW calculation, which does not take into account EA processes, underestimate the experimental data by more than 100% in the region before the cross section maximum. If EA processes are taken into account the CADW calculation is in very good agreement with the experimental data. Ten different excitations are considered with the $3p \rightarrow 4p$ excita-

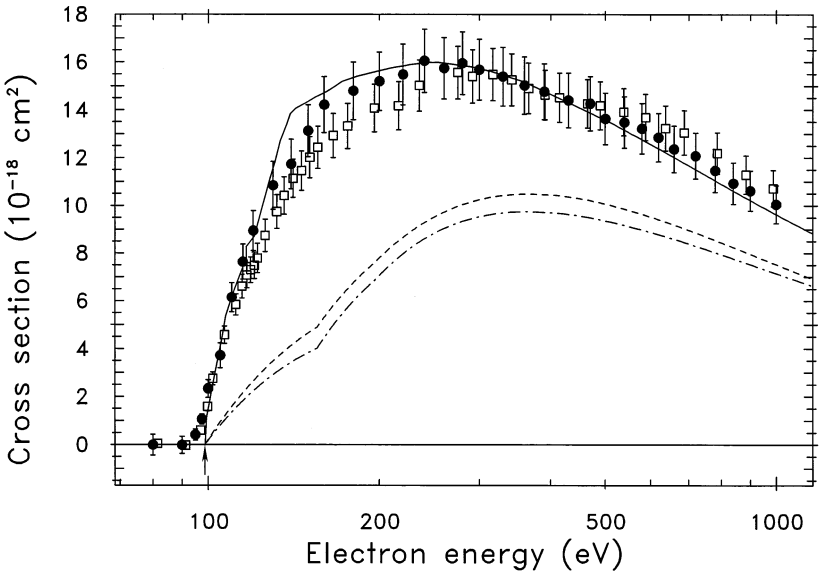


Fig. 6. Cross section for the electron-impact single ionization of $Fe^{5+}$ ions. Circles: present measurements, squares: measurement of Gregory et al. [9]. Error bars represent total experimental uncertainties. The arrow indicates the calculated ionization threshold of the ground state. Dashed line: CADW calculation (Pindzola et al. [12] for direct ionization from the $3d^3$ ground state configuration. Solid line: CADW calculation for total cross section including direct ionization from the 3*d*, 3*p*, and 3*s* shells and excitation autoionization from 3*d*, 3*p*, and 3*s* shells. Dashed-dotted line: Lotz formula [22]. CADW calculation for direct ionization and Lotz formula include the outermost 3*d*, 3*p*, and 3*s* shells.

tion being the strongest. Further important contributions are made by $3s \rightarrow 3d$ and $3p \rightarrow 4d$ excitations. From the good agreement of the CADW calculation with the experimental data and the established power of such calculations we conclude that excitation-autoionization processes play a very important role for the single ionization of $Fe^{5+}$ ions.

### *3.2. Double ionization*

The measured cross section for electron-impact double ionization of $Fe^{5+}$ ions is shown in Fig. 7. The measurements have been carried out employing our high-current electron gun from the respective threshold region up to electron energies of 1 keV. Using the high-energy electron gun, the measurements have been extended up to energies of 5 keV. The data points in the overlap region of both guns are in very good agreement. The onset of the measured cross section agrees well with the calculated ionization threshold of 224.1 eV. In the cross section function a second rise of the curve is observed at around 700 eV which is correlated with inner-shell effects. The bars in the upper part of Fig. 7 indicate the energy range for EDA of 2*p* and 2*s* electrons, whereas the arrow at the end of each bar indicates the ionization threshold of the 2*p* and 2*s* electrons, respectively. The rise in the cross section occurs at the calculated lowest $2p \rightarrow 3d$ excitation energy of 712.5 eV.

The measured cross section is compared with the semiempirical formula by Shevelko and Tawara [5,6] and the second scaling law by Fisher et al. [4]. None of the formulae can predict the rise in the cross section caused by inner-shell processes. Both of them give only a very rough estimation of the cross section. In one case [4], the predicted cross section had to be scaled down by a factor of four in order to bring it on scale. Clearly, a further improvement of these predictor formulae seems to be necessary.

In order to investigate indirect ionization processes such as RETA, which occur as sharp structures in the cross section, we have employed our high resolution

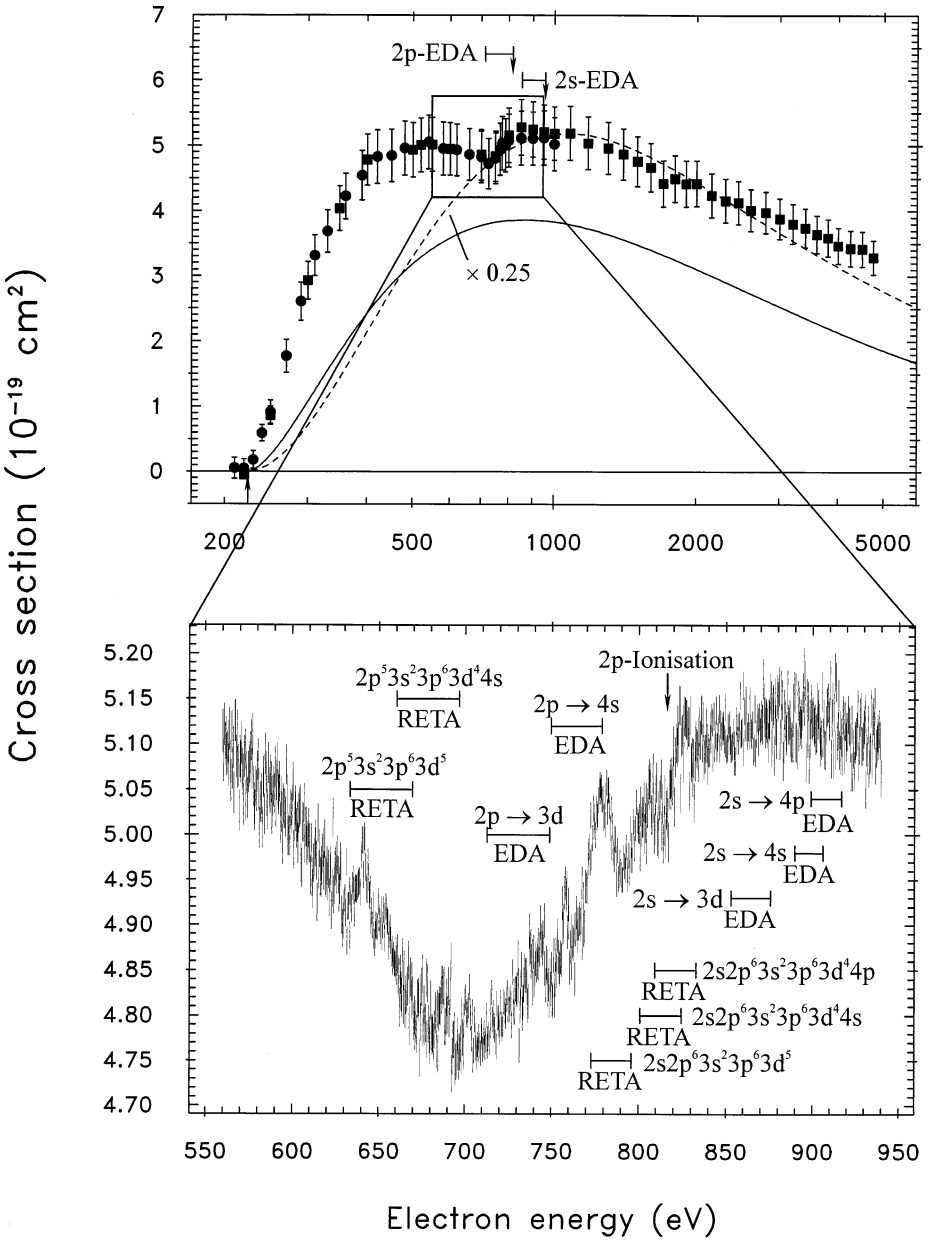


Fig. 7. Cross section for the electron-impact double ionization of $Fe^{5+}$ ions. Upper part: the arrow indicates the ionization threshold of the ground state, error bars indicate total experimental uncertainties. Full curve: semiempirical formula of Bélenger et al. [6]; broken curve: second scaling law by Fisher et al. [4]. Bars: energy range for excitations of the 2*s* and 2*p* electrons from the ground state configuration; arrows at the end of the bars: ionization threshold of the 2*s* and 2*p* electrons, respectively. Lower part: high resolution measurement using the energy-scan technique. Error bars indicate the statistical error. Bars: calculated energy ranges for EDA and RETA processes, respectively.

energy-scan technique. In the energy range 560–940 eV we obtained data, shown in the lower part of Fig. 7, with an energy resolution of a few eV and statistical errors of 0.1%. In order to further reduce the statistical uncertainties we have combined bins of 11 adjacent energy points to give one cross section. Some calcu-

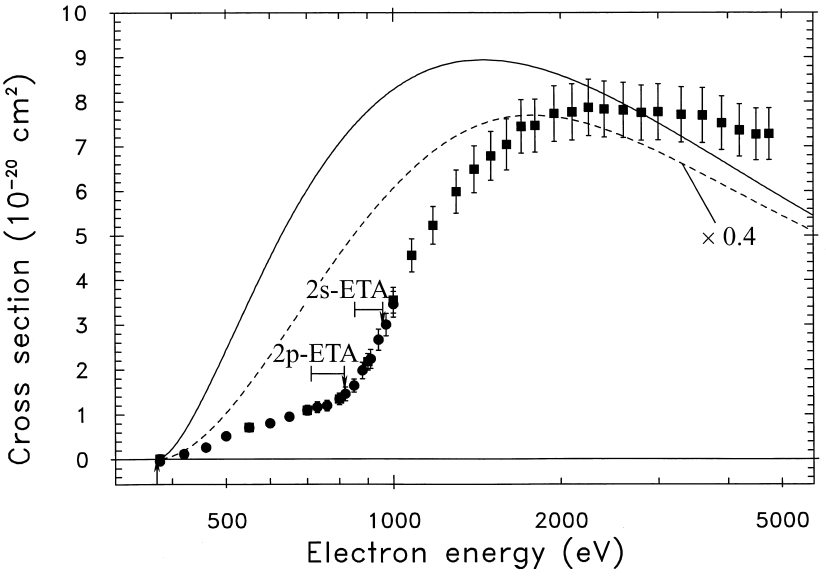


Fig. 8. Cross section for the electron-impact triple ionization of $Fe^{5+}$ ions. Error bars represent the total experimental uncertainties. The arrow indicates the ionization potential of the ground state. Bars: energy range for excitations of the 2*s* and 2*p* electrons from the ground state configuration; arrows at the end of the bars: ionization potential of 2*s* and 2*p* electrons, respectively. Full curve: semiempirical formula of Shevelko and Tawara [5]; dashed curve: second scaling law by Fisher et al. [4].

lated energy ranges resulting from EDA or RETA processes are indicated by bars in the lower part of Fig. 7. The energy-scan measurement reveals many features that are not visible in the upper part of Fig. 7. The enhancement of the cross section matches the calculated threshold of the $2p \rightarrow 3d$ excitation at 712.5 eV. If one considers that the 180 levels of the excited state configuration spread over an electron energy range of about 36 eV, it is not surprising that the $2p \rightarrow 3d$ EDA process does not appear as a sharp step but as a continuous rise in the cross section. Going to higher energies further EDA processes become possible (e.g. $2p \rightarrow 4s$ EDA), until the 2*p*-ionization threshold is reached at 816.3 eV.

If we look at the lowest resonant process of 2*p* electrons (resonant capture of the projectile electron into the 3*d* shell with simultaneous excitation of a 2*p* electron into the 3*d* shell followed by triple autoionization), a clear peak can be observed at about 640 eV. Another most remarkable resonant structure is observed at the lowest energy for resonant excitation of 2*s* electrons (773.1 eV, $Fe^{4+}$ $2s2p^6 3s^2 3p^6 3d^5$). Although this resonant structure is observed above the series limit for resonant $2p \rightarrow 3d$ excitation

$$e^- + Fe^{5+}(2p^6 3s^2 3p^6 3d^3) \rightarrow Fe^{4+}(2p^5 3s^2 3p^6 3d^4 nl) \qquad \text{with } n \geq 3$$

it cannot be associated unambiguously with a resonant 2*s* excitation, because further resonant 2*p* excitations such as

$$e^- + Fe^{5+}(2p^6 3s^2 3p^6 3d^3) \rightarrow Fe^{4+}(2p^5 3s^2 3p^6 3d^3 nln'l') \qquad \text{with } n,\ n > 3$$

are possible up to the 2*p*-ionization threshold. However, to reach an excitation energy of ~780 eV, both electrons would have to be excited into outer shells. Because excited states are closely spaced for higher

Table 1
Ionization energies of $Fe^{5+}$ ions (eV) [20]

| Configuration | Single ionization | Double ionization | Triple ionization |
|---|---|---|---|
| $Fe^{5+}$ $3s^2 3p^6 3d^3$ | 98.16 | 224.1 | 375.1 |

Table 2
Ionization energies of inner-shell electrons and excitation energies of some configurations relative to the $3s^2 3p^6 3d^3$ ground state configuration of $Fe^{5+}$ for double ionization [20]

| Configuration | Process | Number of final state levels | Excitation energy (eV) |
|---|---|---|---|
| $Fe^{4+}$ $2p^5 3s^2 3p^6 3d^5$ | resonant $2p$ excitation | 214 | 633.4–669.3 |
| $Fe^{4+}$ $2p^5 3s^2 3p^6 3d^4 4s$ | resonant $2p$ excitation | 360 | 660.3–696.9 |
| $Fe^{5+}$ $2p^5 3s^2 3p^6 3d^4$ | $2p \rightarrow 3d$ excitation | 180 | 712.5–748.7 |
| $Fe^{5+}$ $2p^5 3s^2 3p^6 3d^3 4s$ | $2p \rightarrow 4s$ excitation | 213 | 749.5–778.9 |
| $Fe^{6+}$ $2p^5 3s^2 3p^6 3d^3$ | $2p$ ionization | | 816.3 |
| $Fe^{4+}$ $2s2p^6 3s^2 3p^6 3d^5$ | resonant $2s$ excitation | 74 | 773.1–796.0 |
| $Fe^{4+}$ $2s2p^6 3s^2 3p^6 3d^4 4s$ | resonant $2s$ excitation | 126 | 801.1–824.7 |
| $Fe^{4+}$ $2s2p^6 3s^2 3p^6 3d^4 4p$ | resonant $2s$ excitation | 360 | 809.4–833.1 |
| $Fe^{5+}$ $2s2p^6 3s^2 3p^6 3d^4$ | $2s \rightarrow 3d$ excitation | 63 | 853.2–875.8 |
| $Fe^{5+}$ $2s2p^6 3s^2 3p^6 3d^3 4s$ | $2s \rightarrow 4s$ excitation | 74 | 889.9–906.2 |
| $Fe^{5+}$ $2s2p^6 3s^2 3p^6 3d^3 4p$ | $2s \rightarrow 4p$ excitation | 213 | 899.2–916.8 |
| $Fe^{6+}$ $2s2p^6 3s^2 3p^6 3d^3$ | $2s$ ionization | | 956.7 |

excitation energies, a series of small peaks, which cannot be resolved experimentally, are expected rather than one strong resonance peak. Thus, the structure observed at about 780 eV is most likely due to resonant $2s$ excitation.

### 3.3. Triple ionization

The measured cross section for triple ionization of $Fe^{5+}$ ions from the threshold up to 5 keV is displayed in Fig. 8. As in the case of the double ionization, a perfect agreement can be observed in the overlapping energy range of the two electron guns used. The horizontal bars indicate the energy ranges for ETA processes of $2p$ and $2s$ electrons, respectively. The ionization thresholds of these inner-shell electrons are indicated by arrows at the end of each bar. For energies higher than these thresholds the process of inner-shell ionization with subsequent double autoionization contributes to the triple ionization cross section. The steep onset in the cross section function matches very well with the calculated $2p$ inner-shell ionization threshold at 816.3 eV. Above this threshold the cross section is completely dominated by inner-shell contributions and increases rapidly from 1.4 $10^{-20}$ $cm^2$ to 7.8 $10^{-20}$ $cm^2$ in the cross section maximum.

The curves in the figure represent the semiempirical predictions by Shevelko and Tawara [5] (full curve) and by Fisher et al. [4] (dashed curve). As in the case of double ionization, no predictor formula matches the experimental data. Both formulae mainly overestimate the cross section in the investigated energy range. Because of the very low cross section (1.4 $10^{-20}$ $cm^2$ at 816.3 eV) we have not been able to apply the energy-scan technique for searching in a tolerable measurement time and with good statistics for the expected narrow structures in the cross section, which may occur in the vicinity of the $2s$ and $2p$ thresholds.

## 4. Conclusions

We have studied single, double, and triple ionization of $Fe^{5+}$ ions by electron impact. For single ionization, the measured cross sections are in very good agreement with previous experimental data and also with CADW calculations if excitation-autoionization processes are taken into account by theory. The cross sections for double and triple ionization show significant, respectively dominant contributions of inner-shell processes. Using a high-resolution energy-scan technique, we could resolve narrow structures in the double ionization cross section resulting from excitation-double-autoionization and resonant-excitation-triple-autoionization processes. Comparison of the multiple ionization cross sections with

semiempirical predictor formulae shows that further improvement of those approaches is necessary.

## Acknowledgement

Support by Deutsche Forschungsgemeinschaft (DFG), Bonn-Bad Godesberg, is gratefully acknowledged.

## References

[1] M. Tendler, K. Lackner, R. Wunderlich, Phys. Lett. A 106 (1984) 420–422.
[2] A. Müller, Phys. Lett. A 113 (1986) 415–419.
[3] M. Stenke, K. Aichele, D. Hathiramani, G. Hofmann, M. Steidl, R. Völpel, V.P. Shevelko, H. Tawara, E. Salzborn, J. Phys. B: At. Mol. Opt. Phys. 28 (1995) 4853–4859.
[4] V. Fisher, Y. Ralchenko, A. Goldgirsh, D. Fisher, Y. Maron, J. Phys. B: At. Mol. Opt. Phys. 28 (1995) 3027–3046.
[5] V.P. Shevelko, H. Tawara, J. Phys. B: At. Mol. Opt. Phys. 28 (1995) L589–594.
[6] C. Bélenger, P. Defrance, E. Salzborn, V.P. Shevelko, H. Tawara, D.B. Uskov, J. Phys. B: At. Mol. Opt. Phys. 30 (1997) 2667–2679.
[7] R.G. Montague, M.J. Diserens, M.F.A. Harrison, J. Phys. B: At. Mol. Phys. 17 (1984) 2085–2090.
[8] D.W. Mueller, T.J. Morgan, G.H. Dunn, D.C. Gregory, D.H. Crandall, Phys. Rev. A 31 (1985) 2905–2913.
[9] D.C. Gregory, F.W. Meyer, A. Müller, P. Defrance, Phys. Rev. A 34 (1986) 3657–3667.
[10] D.C. Gregory, L.J. Wang, F.W. Meyer, K. Rinn, Phys. Rev. A 35 (1987) 3256–3264.
[11] J. Linkemann, A. Müller, J. Kenntner, D. Habs, D. Schwalm, A. Wolf, N.R. Badnell, M.S. Pindzola, Phys. Rev. Lett. 74 (1995) 4173–4176.
[12] M.S. Pindzola, D.C. Griffin, C. Bottcher, S.M. Younger, H.T. Hunter, Nucl. Fusion Suppl. (1987).
[13] H. Wollnik, J. Brezina, M. Berz, Nucl. Instr. Meth. Phys. Res. A 258 (1987) 408–411.
[14] R. Becker, A. Müller, C. Achenbach, K. Tinschert, E. Salzborn, Nucl. Instr. Meth. Phys. Res. B 9 (1985) 385–388.
[15] M. Stenke, K. Aichele, D. Hathiramani, G. Hofmann, M. Steidl, R. Völpel, E. Salzborn, Nucl. Instrum. Methods Phys. Res. B 98 (1995) 573–576.
[16] W.B. Herrmannsfeldt, SLAC-166 Electron Trajectory Program, Stanford 1973.
[17] A. Müller, K. Tinschert, C. Achenbach, E. Salzborn, Nucl. Instrum. Methods Phys. Res. B 10/11 (1985) 204–206.
[18] A. Müller, K. Tinschert, G. Hofmann, E. Salzborn, G.H. Dunn, Phys. Rev. Lett. 61 (1988) 70–73.
[19] A. Müller, G. Hofmann, B. Weissbecker, M. Stenke, K. Tinschert, M. Wagner, E. Salzborn, Phys. Rev. Lett. 63 (1989) 758–761.
[20] I.P. Grant, B.J. McKenzie, P.H. Norrington, D.F. Mayers, N.C. Pyper, Comp. Phys. Comm. 21 (1980) 207–231.
[21] B.J. McKenzie, I.P. Grant, P.H. Norrington, Comp. Phys. Comm. 21 (1980) 233–246.
[22] R.D. Cowan, The Theory of Atomic Structure and Spectra, Berkeley, CA, 1981.
[23] W. Lotz, Z. Phys. 216 (1968) 241–247.